Open Access

Repository of the Max Delbrück Center for Molecular Medicine (MDC) in the Helmholtz Association

https://edoc.mdc-berlin.de/14763/

Cavin 1 function does not follow caveolar morphology

Timmel T., Kunz S., Seifert F., Schuelke M., Spuler S.

This is a copy of the accepted manuscript, as originally published online ahead of print by the American Physiological Society. The original article has been published in final edited form in:

American Journal of Physiology Cell Physiology
2015 JUN 15 ; 308(12): C1023-C1030
2015 APR 22 (first published online)
doi: 10.1152/ajpcell.00329.2014

Publisher: American Physiological Society

Copyright © 2015 the American Physiological Society

1
2 # Cavin1 function does not follow caveolar morphology
3
4 Tobias Timmel[1]*, Séverine Kunz[1]*, Franziska Seifert[2], Markus Schuelke[2], Simone Spuler[2]
5
6 *contributed equally
7
8 [1]Muscle Research Unit, Experimental and Clinical Research Center, a joint cooperation between the
9 Charité Medical Faculty and the Max Delbrück Center for Molecular Medicine Berlin, Germany
10 [2]Department of Neuropediatrics and NeuroCure Clinical Research Center, Charité Universitätsmedizin
11 Berlin
12
13 **Running title:**
14 Caveolar function and morphology
15
16 **Key words:**
17 caveolae, caveolin, cavin 1/PTRF, FACS, electron microscopy
18
19 **Correspondence:**
20 Dr. Simone Spuler, Muscle Research Unit, Experimental and Clinical Research Center, a joint
21 cooperation between the Charité Medical Faculty and the Max Delbrück Center for Molecular
22 Medicine, Lindenberger Weg 80, 13125 Berlin, Germany;
23 T: +49 30 450 540501; F: +49 30 450 540907; e-mail: simone.spuler@charite.de
24
25
26 **Counts**:
27 Abstract: 165 words
28
29

Abstract

The function of caveolae, small invaginations of the plasma membrane, remains a matter of debate. Endocytosis and compartmentalization of metabolic and signaling pathways are discussed. Caveolin 3 and PTRF are two important proteins that ensure shaping of caveolae in muscle cells. We investigated caveolae morphologically by electron microscopy in human myotubes obtained from patients with *CAV3* mutations and did functional analyses in human fibroblasts derived from a patient with a mutation in *PTRF*. We found that despite the complete clinical picture of a caveolinopathy the caveolin 3-deficient myotubes displayed normal caveolae in shape and number. Further, PTRF-deficient fibroblasts devoid of caveolae took up cholera toxin B differently in comparison to normal fibroblasts. However, after caveolae were rescued by transfection of PTRF, the cholera toxin B uptake did not normalize. We conclude that the presence of caveolae as an anatomical structure is not sufficient to ensure their proper function. Alternatively, the functional properties assigned to caveolae might be mediated by different mechanisms yet to be resolved.

Introduction

Caveolae are vesicular structures that can open up to the outer cell membrane and are there identified as flask-like invaginations. They are 25 to 100 nm in size and are encountered on numerous mammalian cell types such as adipocytes, myocytes and fibroblasts. Caveolae are characterized by the presence of scaffolding proteins, the most important being caveolin and the family of cavins. There are three caveolin proteins. Caveolin 3 (CAV3) is specific for muscle, caveolin 1 (CAV1) is present on all other caveolae-bearing cell types. There are four cavin proteins. Cavin 1, subsequently named polymerase I and transcript release factor (PTRF), appears to be a very good marker for caveolae because PTRF binds to CAV1 only when caveolae are fully assembled at the cell membrane (3). The function of caveolae is not resolved. They probably are involved in endocytosis and the formation of the t-tubular structure in muscle cells. However, the dynamics of caveolar endocytosis, the cargo transported through caveolae or the cell type specificity of caveolae are not clear (8). It has also been shown that caveolae maintain a plasma membrane reservoir to adjust changes in cell volume (15).

Several diseases are associated with mutations in genes encoding the caveolins and PTRF. If *PTRF* is mutated affected patients suffer from muscular dystrophy with the rippling muscle phenomenon, lipodystrophy, hypertrophy of the striated and smooth muscle, cardiac conduction defects as well as endocrinological abnormalities (13). Mutations in *CAV3* lead to mild to moderate muscle weakness, muscle rippling, often myalgias and sometimes cardiomyopathy (limb girdle muscular dystrophy 1A; LGMD1A). Mutations in *CAV1* are associated with cancer (10). Whether these diseases and symptoms are caused by the absence of caveolae and subsequent disturbances of endocytosis or whether a role of the affected proteins independent of the anatomical structure of "caveolae" is responsible is unresolved.
We investigated caveolae in human *CAV3* and *PTRF* mutations morphologically and functionally.

Materials and methods

Cells, cell culture, and transfection

Primary myoblasts were isolated from patients with mutations in *CAV3* and immortalized as described before (12). The cell line established in our lab harbored a heterozygous mutation in exon 1 (c.80G>A, p.R27E). Another cell line was derived from a patient with a heterozygous mutation in exon 1 (c.83C>T, p.P28L) and provided by Dr. Vincent Mouly (UPMC, Paris, France). The muscle cells were cultivated in a CO_2-incubator (BBD 6220, Thermo Fischer Scientific, Schwerte, Germany) at 37 °C with 5 % CO_2 and 96 % relative humidity. As proliferation medium, Skeletal Muscle Cell Growth Medium (Provitro, Berlin, Germany) complemented with 10 % fetal calf serum (Biochrom, Germany), 1.5 % GlutaMax (Gibco/Life, Darmstadt, Germany) and 40 µg/ml gentamycin (Gibco) was used. Myoblasts were grown to 80-90 % confluence and subsequently switched to differentiation medium (Opti-MEM® I (1x), Gibco) for 4-6 days.
Primary human fibroblasts lacking polymerase I and transcript release factor (PTRF, c.362dupT) and fibroblasts from healthy controls (13) were cultured in DMEM (Gibco). The medium contained 10 % fetal calf serum and gentamycin (40 µg/ml).
We transfected fibroblasts one day after plating either by microinjection or by lipofection. The plasmid DNA used for the experiments was human *PTRF* cloned into pEGFP-N3 vector (Clontech Laboratories, Mountain View, CA, USA). We diluted the plasmid DNA in ultrapure water to a final concentration of 0.05 µg/µl and 1 µg/µl, respectively. One day after transfection we controlled protein expression by eGFP

epifluorescence. For microinjection, we seeded fibroblasts onto culture dishes with a cover glass bottom (FD35, World Precision Instruments, Berlin Germany). We transfected the cells with a FemtoJet system (Eppendorf, Wesseling-Berzdorf, Germany) combined with the InjectMan NI2 (Eppendorf). After centrifugation at 4 °C for 30 min we loaded the supernatant immediately onto the capillaries (Femtotip II, Eppendorf). Microinjections into the cytoplasm of fibroblasts were done with an injection pressure of 150 hPa. For lipofection, we plated fibroblasts in 6-well plates (TPP, Cotech, Berlin, Germany). We added 200 µl/well serum-free DMEM containing 1 µl plasmid DNA and 2 µl transfection reagent (X-tremeGENE HP, Roche, Mannheim, Germany). One day after transfection we controlled protein expression and calculated the transfection rate (2-5 %).

RT-qPCR

After extraction from cultured skin fibroblasts, primary and immortalized myotubes using (TriZol? Which kit?), 500 ng of total RNA were reversely transcribed into cDNA using the Superscript® III kit (Life Technologies) with random hexamers. RT-qPCR reactions were run in triplicate on an ABI7700 System (Applied Biosystems) using the SYBR® green (Life Technologies) chemistry with the following oligonucleotide primer pairs: (CAV1) FORW 5'-CGT GGT CAA GAT TGA CTT TGA A-3', REV 5'-CAC AGT GAA GGT GGT GAA GC-3'; (CAV3) FORW 5'-GAG GAC ATA GTC AAG GTG GA-3', REV 5'-TGT AGC TCA CCT TCC ACA C-3'; (PTRF) FORW 5'-AGA TCA AGA AGC TGG AGG T-3', REV 5'- AGC TTC ACT TCA TCC TGG T-3'. The primers were chosen to comprise all known splice isoforms of the genes. 18S rRNA, GAPDH and HPRT were used as reference genes as described (6). In order to be able to calculate amplification ratios between test- and reference-genes using the PCR-efficiency corrected –ΔΔCt method (11), we first determined the efficiency of each PCR reaction with a 1:10 standard dilution series as described.

CTxB uptake assay

For subsequent immunofluorescence and fluorescence imaging, we plated fibroblasts in 8-well chamber slides (Nunc LabTek, Thermo Fischer Scientific). Three days after plating we incubated the cells for 5, 10 or 15 min at 37 °C with Alexa Fluor 555 labeled CTxB (Molecular Probes/Life, Darmstadt, Germany) at a concentration of 200 ng/ml in cell culture media. Fibroblasts intended for FACS experiments were seeded onto 6-well plates. We incubated the cells with Alexa Fluor 488 or 647 labeled CTxB (Molecular Probes) at 37 °C and at a concentration of 400 ng/ml in cell culture media. CTxB incubation times were set to 2 min, 15 min, and/or 60 min. For the starving assay, the labeled CTxB was diluted in glucose-free HEPES buffered Krebs-Ringer solution (1 mM $CaCl_2$, 5 mM NaOH, 25 mM HEPES, 135 mM NaCl, 3.6 mM KCl, 0.5 mM K_2HPO_4, 0.5 mM $MgSO_4$, pH=7.4). Furthermore, we pre-incubated fibroblasts before CTxB treatment either in DMEM including supplements or in glucose-free Krebs-Ringer HEPES buffer.

Immunofluorescence

We washed fibroblasts with PBS (Gibco) and fixed them in 3.7 % formaldehyde-PBS solution for 12 min at room temperature (RT). After repeated washing in PBS we permeabilized the cells with 0.2 % Triton X-100 in PBS for 2 min. We washed the cells with PBS and applied for 30 min 1 % BSA (Carl Roth, Karlsruhe, Germany) in PBS for blocking. We incubated the primary antibodies in PBS containing 1 % BSA for 60 min at RT. After thorough washing with PBS we incubated the cells with the secondary antibodies for 60 min at RT in 1 % BSA in PBS. After the washing procedure we stained the nuclei with Hoechst 33342 (Invitrogen/Life, Darmstadt, Germany) diluted 1:2,000 in 1 % BSA in PBS for 3 min at RT. After a final washing procedure we mounted the samples in Aqua PolyMount (Polysciences, Eppelheim, Germany). We applied the primary antibodies at the following dilutions: monoclonal antibody to Cav1 (sc-53564, Santa Cruz, Heidelberg, Germany) at 1:200 and polyclonal antibody to Cav1 (ab2910, Abcam, Cambridge, UK) at 1:250. As secondary antibodies we used anti-mouse Alexa Fluor 488 and anti-rabbit Alexa Flour 647 (Molecular Probes) at 1:500.

FACS experiments

Before FACS analysis fibroblasts were washed in PBS and fixed in 3.7 % formaldehyde-PBS solution for 12 min at RT. To increase the sample size we pooled identically treated wells and analyzed them in a BD FACSCanto (Becton Dickinson, Sparks, MD, USA). We evaluated the resulting data using FlowJo 10.0.7 software (TreeStar, Ashland, OR, USA). For further post-processing of the FACS data and for statistics we used the R software version 3.1 (16). FACS gating parameters were set to selectively assess eGFP-positive or -negative cells.

Atomic force microscopy, confocal imaging, and image processing

The day after microinjection we fixed the fibroblasts in 3.7 % formaldehyde-PBS solution for 12 min at RT. After thorough washing in PBS we transferred the dish to the AFM stage. We used a Nanowizard II atomic force microscope (JPK Instruments, Berlin, Germany) mounted to a confocal laser-scanning microscope (LSM 700, Zeiss, Göttingen, Germany). Prior to each experiment we applied the thermal noise method to calibrate the cantilever (4). The AFM was operated in contact mode under liquid (PBS). A Petri dish heater (JPK Instruments) kept the temperature constant at 25 °C. A translucent and uncoated soft silicon nitride cantilever with a silicon tip (Hydra 2R-100N, Applied NanoStructures, Mountain View, CA, USA) was chosen. The cantilever had a nominal spring constant of 0.011 N/m and a resonant frequency of 21 kHz. Immediately after taking a bright-field image of the cantilever tip and a fluorescence image of the sample, AFM scanning was started. We acquired the scans at a force setpoint of 0.3 nN and a line rate of 1 Hz.

The AFM data were processed with JPK Data Processing 4.2 software (JPK Instruments) and Gwyddion software (9). We removed very few isolated streaks by line interpolation and enhanced the image contrast by slope correction resulting in image flattening. To visualize fine structures, we fitted a polynomial to the entire height image and subtracted this background slope from the image. We combined and overlaid confocal and AFM images using the cantilever tip as landmark (17).

For confocal imaging, we used the Zeiss LSM 700 confocal microscope equipped with a LCI Plan-Neofluar 63x/1.3 glycerol immersion lens (Zeiss). For the quantification of fluorescence intensities we took 8-10 images per cell type and treatment using a LD Plan-Neofluar 40x/0.6 lens (Zeiss). We processed the fluorescence images with the Fiji distribution of ImageJ (14) adjusting brightness and contrast, removing background noise, and applying Gaussian smoothing. Next, we measured the cumulated fluorescence intensities per image and normalized the result to the respective number of nuclei. Using the R software (16) we calculated the statistical significance of the quantified fluorescence intensities. Finally, we assembled all images and graphs in Adobe Illustrator CS5 software (Adobe Systems, Dublin, Ireland).

Transmission electron microscopy

Three days after sorting by FACS we processed cells for conventional electron microscopy. Adherent fibroblasts and myotubes or FACS-sorted eGFP-positive fibroblasts were fixed for 2 hours in 2.5 % glutaraldehyde at pH 7.4. Due to the low amount of cells, FACS-sorted fibroblasts were resuspended in 10 % gelatin and pelleted. The gelatin was solidified at 4 °C for 30 min. Subsequently, we sectioned the cell pellet to 1 mm^3 cubes and processed them further for Epon embedding. Adherent and gelatin-embedded cells were postfixed with 1 % osmium tetroxide, gradually dehydrated in ethanol and embedded in Epon resin. Ultrathin sections were cut using an ultramicrotome (Ultracut S, Reichert Division of Leica, Vienna Germany), stained with uranyl acetate and lead citrate, and observed under a transmission electron microscope (EM 910, Zeiss, Oberkochen, Germany). Pictures were taken with a CDD camera (Quemesa, Olympus Soft Imaging Solutions, Münster, Germany) integrated in the imaging software iTEM (version 5.2, Olympus Soft Imaging Solutions).

Selection criteria for quantification of caveolae in myotubes were: (i) contrasted and sharp plasma membrane, (ii) fully accessible transversal or longitudinal sections, (iii) lack of strong artefacts from fixation as vacuoles, extracted organelles and raptured cells. As morphological differentiation markers, the presence of more than two nuclei (2) was defined for quantification (Fig. 1B). For every cell line 10-13 myotubes of one embedding preparation were analyzed and a minimum of 600 µm plasma membrane per cell line was quantified. Pictures at a magnification of 5,000 were acquired and analyzed with the iTEM software. The length of the plasma membrane and the amount of distinct endocytic structures were quantified. Statistical analyses were done using R software version 3.1 (16).

Results and Discussion

***CAV3* mutants in human skeletal muscle lead to severe reduction of CAV3 protein but caveolae decorate the sarcolemma normally.**

Serial sections obtained from muscle biopsy specimens from patients with heterozygous mutations in *CAV3* (p.P28L and p.R27E, respectively) demonstrate a mild myopathy with a slight increase in connective tissue components and a severe reduction in CAV3 protein expression (Fig. 1A). We then quantified caveolae in human myotubes obtained from the same patients with *CAV3* mutations by electron microscopy. Myotubes for quantification were carefully selected using predefined criteria (see Material and Methods) (Fig. 1B, C). The number of open caveolae in normal

myotubes and in myotubes carrying *CAV3* mutations was almost identical (Fig. 1D). The morphology of individual caveolae was also not different between normal and *CAV3* mutant myotubes. One could argue that caveolae form nevertheless because only one *CAV3* allele is mutated in autosomal-dominant LGMD1A. However, the number of caveolae was not reduced accordingly. Apparently, caveolae form even if CAV3 is severely reduced.

Mutation in one structural component of the caveolae (e.g. caveolin or cavin) is not compensated by mRNA up-regulation of the other components.

Despite the presence of a heterozygous mutation in *CAV3*, the *CAV3*-mRNA copy number did not differ significantly between immortalized *CAV3*$^{+/-}$ and control myotubes (Fig. 2). The primary myotubes of the controls had a varying tendency towards higher *CAV3*-mRNA copy numbers (ratio 1.2-2.5, depending on the reference gene).
The *CAV1* and *PTRF*-mRNA copy numbers in mutant *CAV3*$^{+/-}$ myotubes were not compensatory up-regulated.
The *PTRF*-mRNA transcripts in *PTRF*$^{-/-}$ mutant fibroblasts were grossly reduced in comparison to control fibroblasts, probably due to nonsense-mediated messenger decay secondary to the frame-shift mutation c.362dupT. Depending on the chosen reference gene, *CAV1*-mRNA transcripts were only inconsistently upregulated (if referred to *GAPDH* and *HPRT*) or remained unchanged (if referred to *18S rRNA*). CAV3-mRNA transcripts were absent in both control and *PTRF*$^{-/-}$ mutant fibroblasts.
Taken together, all three proteins seem to participate in the formation and function of the caveolae in different contexts and cannot easily compensate for each other.

Uptake of cholera toxin in human PTRF-negative fibroblasts is distinct from healthy fibroblasts.

To gain further insight into the impact of caveolae on endocytosis we selected human fibroblasts with a mutation in *PTRF* that are completely devoid of caveolae and compared these with normal fibroblasts (Fig. 1D) (13). As a model we chose the uptake of cholera toxin subunit B (CTxB). CTxB is enriched and internalized by caveolae but also diffuses into cells in the absence of caveolae (1, 5). First, fluorescently labeled CTxB was followed on the single cell level using confocal microscopy (Fig. 3). After CTxB uptake, cells were fixed and co-stained with anti-CAV1 ab. In healthy *PTRF*$^{+/+}$ fibroblasts CAV1 and CTxB co-localized clearly at the membrane and also at intracellular structures. In contrast, *PTRF*$^{-/-}$ fibroblasts displayed a diffuse distribution pattern of CTxB and no co-localization of CAV1 and CTxB (Fig. 3).

High-throughput FACS analysis is suitable to detect differences in CTxB uptake dependent on caveolae.

Attempts to quantify CTxB uptake by measurement of fluorescence intensities in confocal images was found to be difficult and rather subjective. We therefore developed an alternative strategy to quantify CTxB uptake not on the single cell level but rather as a high-throughput strategy. We incubated human *PTRF*$^{+/+}$ and *PTRF*$^{-/-}$ fibroblasts with Alexa-488-CTxB for 15 min and analyzed the cells by fluorescence-activated cell sorting (FACS). Now, the intensity distribution represented by density curves and box plots showed significant differences in CTxB uptake (Fig. 4A). In *PTRF*$^{-/-}$ fibroblasts the mean intensity was significantly lower than in healthy controls (13,885 vs. 24,455, $p < 0.001$). Further, the distribution of CTxB uptake had characteristic differences between *PTRF*$^{+/+}$ and *PTRF*$^{-/-}$ fibroblasts with a distinctive bimodal curve in PTRF-negative cells. These results support the notion that caveolae are important for CTxB uptake.
We wondered if CTxB uptake was dependent on the time of CTxB incubation or on cell culture media components and tested multiple conditions (Fig. 4B). CTxB intensities increased with prolonged incubation time of CTxB, thus the intensity distribution slightly shifted towards higher intensities. We also modified the media by depleting glucose or serum growth factors. The impact of media modification, however, was negligible. The bimodal curve of CTxB uptake in PTRF-deficient cells and the differences to normal fibroblasts remained. Therefore, the differences in subcellular CTxB distributions as well as the distinct uptake characteristics quantified by FACS suggest a role of caveolae in CTxB uptake.

Rescue of PTRF in *PTRF*$^{-/-}$ fibroblasts is sufficient to induce *de novo* formation of caveolae.

If the caveolae account for the differences in CTxB uptake, then a PTRF rescue in *PTRF*$^{-/-}$ cells should alter the uptake behavior and the curve shape of FACS analysis should transform to that seen in normal fibroblasts. Before analyzing the CTxB uptake we verified by three different methods that PTRF rescue was sufficient to induce the formation of caveolae in *PTRF*$^{-/-}$ fibroblasts. First, we transfected *PTRF*$^{-/-}$ fibroblasts with eGFP-tagged hPTRF plasmid DNA. One day after transfection

anti-Cav1 ab and PTRF-eGFP co-localized at the membrane and intracellularly, strongly indicating the presence of caveolae (Fig. 5A).
Next, using combined confocal fluorescence and atomic force microscopy (AFM) we verified that spots of PTRF-eGFP fluorescence matched topographical depressions of the plasma membrane in transfected *PTRF*$^{-/-}$ fibroblasts. The fluorescence image of PTRF-eGFP showed a punctuate pattern, whereas the AFM height image revealed a highly corrugated surface (Fig. 5B). In the overlay of the properly aligned images we could identify eGFP-positive depressions indicating caveolae.
Finally, we demonstrated the presence of caveolae in PTRF-eGFP transfected *PTRF*$^{-/-}$ fibroblasts by electron microscopy (Fig. 5C). Caveolae in FACS-sorted, eGFP-positive fibroblasts were identified and were well distinguishable from clathrin-coated pits, another type of membrane depressions capable of endocytosis.

PTRF rescue does not alter CTxB uptake characteristics in *PTRF*$^{-/-}$ fibroblasts.
Being confident that PTRF rescue induces caveolae formation in *PTRF*$^{-/-}$ fibroblasts, we repeated the FACS analysis to compare uptake of CTxB in *PTRF*$^{-/-}$ fibroblasts with or without PTRF rescue. The characteristic shape of the basic uptake distribution in each cell type remained unchanged after caveolae had formed (Fig. 6A). The proportion of CTxB-negative cells, as defined by the 99.9 % threshold criterion of untreated cells, was not affected by transfection in both groups (Fig 6C). In both, *PTRF*$^{+/+}$ and *PTRF*$^{-/-}$ fibroblasts, overexpression of PTRF led to a slight reduction of CTxB intensities (Fig. 6B). The negative effect of PTRF overexpression on CTxB uptake is in line with a study reporting reduced CTxB trafficking to the Golgi caused by Cav1 overexpression in both, WT and *Cav1*$^{-/-}$ mouse embryonic fibroblasts (5). In contrast, a study on CTxB uptake in Cav1 overexpressing Caco-2 cells, which are otherwise devoid of caveolae, reported no effect (18). The negative effect of overexpression in the *PTRF*$^{-/-}$ cells might be caused by a general negative side-effect of protein overexpression or by the fact that *de novo* generated caveolae do not contribute to the CTxB uptake. Alternatively, a potential negative side effect could mask the positive contribution of caveolae to the CTxB uptake.

Although PTRF transfection induces caveolae formation, the role of caveolae in CTxB uptake upon PTRF overexpression is unclear. Fluorescence analysis on a subcellular level as well as distinct uptake characteristics revealed by FACS, strongly suggest a contribution of caveolae to CTxB uptake. Our hypothesis, that upon PTRF rescue in *PTRF*$^{-/-}$ fibroblasts the uptake characteristics converges to that of control fibroblasts, did not prove true. Our investigation is limited by the fact that we studied human cells only. Suitable animal models would be required to correlate caveolae morphology and function more extensively (7).

Caveolar function does not correlate well with the presence of the mere "caveolae" as an anatomical structure. Our findings can be interpreted in two ways: The presence of caveolae as an anatomical structure is not sufficient to ensure proper caveolar function. This would be the case in patients with *CAV3* mutations as well as after overexpression of PTRF in our *in vitro* model. Alternatively, the functional properties assigned to caveolae are mediated by different mechanisms yet to be resolved.

Acknowledgements

The German Research Foundation (DFG, Clinical Research Group KFO-192 and GK1631 MyoGrad) supported the project. We thank Stephanie Meyer-Liesener, Stefanie Belz, and Adrienne Rothe for excellent technical assistance and the MDC electron microscopy and FACS core facilities for their qualified help. There is no conflict of interest.

References

1. **Day CA, Kenworthy AK**. Mechanisms underlying the confined diffusion of cholera toxin B-subunit in intact cell membranes. *PLoS One* 7: e34923-e34923, 2012.
2. **Frankel DJ, Pfeiffer JR, Surviladze Z, Johnson AE, Oliver JM, Wilson BS, Burns AR**. Revealing the topography of cellular membrane domains by combined atomic force microscopy/fluorescence imaging. *Biophys J* 90: 2404-2413, 2006.
3. **Hill MM, Bastiani M, Luetterforst R, Kirkham M, Kirkham A, Nixon SJ, Walser P, Abankwa D, Oorschot VMJ, Martin S, Hancock JF, Parton RG**. PTRF-Cavin, a conserved cytoplasmic protein required for caveola formation and function. *Cell* 132: 113-124, 2008.
4. **Hutter JL, Bechhoefer J**. Calibration of atomic-force microscope tips. *Review of Scientific Instruments* 64: 1868-1873, 1993.
5. **Kirkham M, Fujita A, Chadda R, Nixon SJ, Kurzchalia TV, Sharma DK, Pagano RE,**

588 Hancock JF, Mayor S, Parton RG. Ultrastructural identification of uncoated caveolin-independent early endocytic vehicles. *J Cell Biol* 168: 465-476, 2005.

6. **Knierim E, Seelow D, Gill E, von Moers A, Schuelke M**. Clinical application of whole exome sequencing reveals a novel compound heterozygous TK2-mutation in two brothers with rapidly progressive combined muscle-brain atrophy, axonal neuropathy, and status epilepticus. *Mitochondrion* 20: 1-6, 2015.
7. **Liu L, Brown D, McKee M, Lebrasseur NK, Yang D, Albrecht KH, Ravid K, Pilch PF**. Deletion of Cavin/PTRF causes global loss of caveolae, dyslipidemia, and glucose intolerance. *Cell metabolism* 8: 310-317, 2008.
8. **Mayor S, Parton RG, Donaldson JG**. Clathrin-independent pathways of endocytosis. *Cold Spring Harb Perspect Biol* 6: 2014.
9. **Necas D, Klapetek P**. Gwyddion: an open-source software for SPM data analysis. *Central European Journal of Physics* 10: 181-188, 2012.
10. **Patani N, Martin LA, Reis-Filho JS, Dowsett M.** The role of caveolin-1 in human breast cancer. *Breast cancer research and treatment* 131: 1-15, 2012.
11. **Pfaffl MW.** A new mathematical model for relative quantification in real-time RT-PCR. *Nucleic Acids Research* 29: 45, 2001.
12. **Philippi S, Bigot A, Marg A, Mouly V, Spuler S, Zacharias U.** Dysferlin-deficient immortalized human myoblasts and myotubes as a useful tool to study dysferlinopathy. *PLoS Curr* 4: RRN1298-RRN1298, 2012.
13. **Rajab A, Straub V, McCann LJ, Seelow D, Varon R, Barresi R, Schulze A, Lucke B, Lützkendorf S, Karbasiyan M, Bachmann S, Spuler S, Schuelke M.** Fatal cardiac arrhythmia and long-QT syndrome in a new form of congenital generalized lipodystrophy with muscle rippling (CGL4) due to PTRF-CAVIN mutations. *PLoS Genet* 6: e1000874-e1000874, 2010.
14. **Schindelin J, Arganda-Carreras I, Frise E, Kaynig V, Longair M, Pietzsch T, Preibisch S, Rueden C, Saalfeld S, Schmid B, Tinevez J-Y, White DJ, Hartenstein V, Eliceiri K, Tomancak P, Cardona A.** Fiji: an open-source platform for biological-image analysis. *Nat Methods* 9: 676-682, 2012.
15. **Sinha B, Köster D, Ruez R, Gonnord P, Bastiani M, Abankwa D, Stan RV, Butler-Browne G, Vedie B, Johannes L, Morone N, Parton RG, Raposo G, Sens P, Lamaze C, Nassoy P.** Cells respond to mechanical stress by rapid disassembly of caveolae. *Cell* 144: 402-413, 2011.
16. **Team RC.** R: A Language and Environment for Statistical Computing. 2014.
17. **Timmel T, Schuelke M, Spuler S.** Identifying dynamic membrane structures with atomic-force microscopy and confocal imaging. *Microsc Microanal* 20: 514-520, 2014.
18. **Torgersen ML, Skretting G, van Deurs B, Sandvig K.** Internalization of cholera toxin by different endocytic mechanisms. *J Cell Sci* 114: 3737-3747, 2001.

Figure captions

Figure 1. Primary human myotubes from skeletal muscle with CAV3 mutations display caveolae at the plasma membrane normal in abundance and shape. (A) Histological staining of skeletal muscle from patients with mutations in *CAV3* (p.P28L; p.R27E) shows a slight increase in connective tissue, reduced levels of CAV3 but normal beta-dystroglycan staining at the sarcolemma. Scale bar: 20 µm. (B) Electron micrograph of a representative multi-nucleated myotube selected for quantification studies, scale bar: 10 µm. (C) The distribution of caveolae (black arrowheads) over the plasma membrane is variable. Scale bar: 1 µm. (D) Morphological and quantitative analysis on caveolae show that shape and abundance are not altered in myotubes from patients with *CAV3* mutations whereas caveolae are absent in *PTRF*$^{-/-}$ deficient fibroblasts. Other endocytic structures as clathrin-coated pits (white arrowheads) are not altered by PTRF-deficiency. Scale bars: 200 nm.

Figure 2. RT-qPCR measurement of relative mRNA copy numbers for *CAV1, CAV3* and *PTRF*. Copy numbers were determined in primary (n=2) and immortalized myotubes (n=2) of controls and CAV3+/- patients (n=2) as well as in PTRF-/-(n=1) and control (n=1) fibroblasts. The horizontal lines depict the mean of each triplicate measurement. The mRNA ratios were expressed in relation to the mRNA copy numbers of GAPDH, HPRT, and 18S rRNA. Mutant cell lines are depicted by red and control cell lines by black symbols. The kind of mutation on the amino acid level is given in the legend.

Figure 3. The uptake and subcellular localization of CTxB in healthy fibroblasts is distinct from fibroblast devoid of caveolae. CAV1 immunostaining after 10 min of incubation with Alexa-555 labeled CTxB. Nuclei are stained with Hoechst. In contrast to *PTRF*$^{-/-}$ fibroblasts CTxB co-localizes with CAV1 in the healthy controls. Scale bars: 5 µm.

Figure 4. The characteristic differences in CTxB uptake do not depend on CTxB incubation time nor on incubation media (starving). (A) Intensity distribution and box plots of Alexa-488 labeled CTxB revealed by FACS analysis. Due to differing sample sizes we show density curves of the control and *PTRF*$^{-/-}$ fibroblasts compared with untreated cells. (B) Density curves of Alexa-488 labeled CTxB of control and *PTRF*$^{-/-}$ fibroblasts dependent on incubation time and incubation media. We tested different pre-incubation conditions (I) and CTxB incubation media (II).

Figure 5. Rescue of PTRF in *PTRF*$^{-/-}$ fibroblasts is sufficient to induce *de novo* formation of caveolae. (A) Immunostaining of CAV1 after transfection of *PTRF*$^{-/-}$ fibroblasts with PTRF-eGFP using microinjection. The inset picture at higher magnification shows partial co-localization of PTRF-eGFP with CAV1. Scale bars: 20 µm. (B) Fixed biological sample imaged with combined confocal and atomic force microscopy. *PTRF*$^{-/-}$ fibroblasts were transfected with PTRF-eGFP. From left to right, the image series shows the fluorescence signal of the eGFP, the AFM height and the background filtered, i.e. flattened height image, and the overlay of fluorescence and filtered height images. Arrowheads depict eGFP spots matching membrane depressions. Scale bars: 1 µm. (C) Electron micrographs of FACS-sorted *PTRF*$^{-/-}$ fibroblasts transfected with PTRF-eGFP. The black arrowheads indicate caveolae and the white arrowheads clathrin-coated pits. Scale bars: 200 nm.

Figure 6. Although slightly reduced, *de novo* formation of caveolae does not alter the typical uptake characteristics of CTxB in *PTRF*$^{-/-}$ fibroblasts. (A) Density curves of Alexa-647 labeled CTxB dependent on CTxB treatment and PTRF-eGFP transfection. (B) Box plots showing the effect of transfection on the intensities of Alexa-647 labeled CTxB in healthy and *PTRF*$^{-/-}$ fibroblasts. (C) Impact of PTRF-eGFP transfection on the proportion of CTxB-negative fibroblasts as defined by the 99.9 % threshold of CTxB untreated cells.

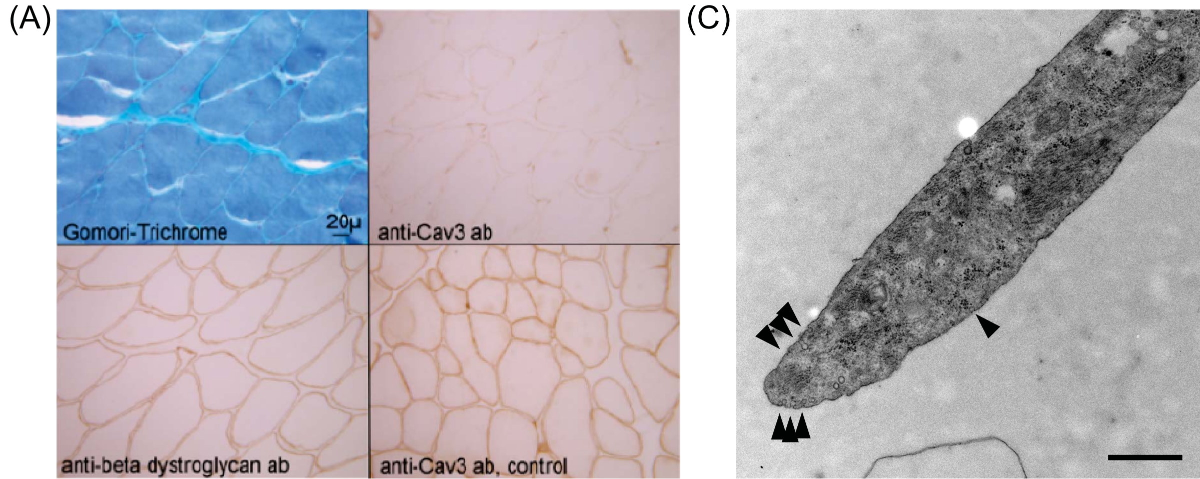
(A)
Gomori-Trichrome
20μ
anti-Cav3 ab
anti-beta dystroglycan ab
anti-Cav3 ab, control
(C)

(B)
N
N
N
N
N
N

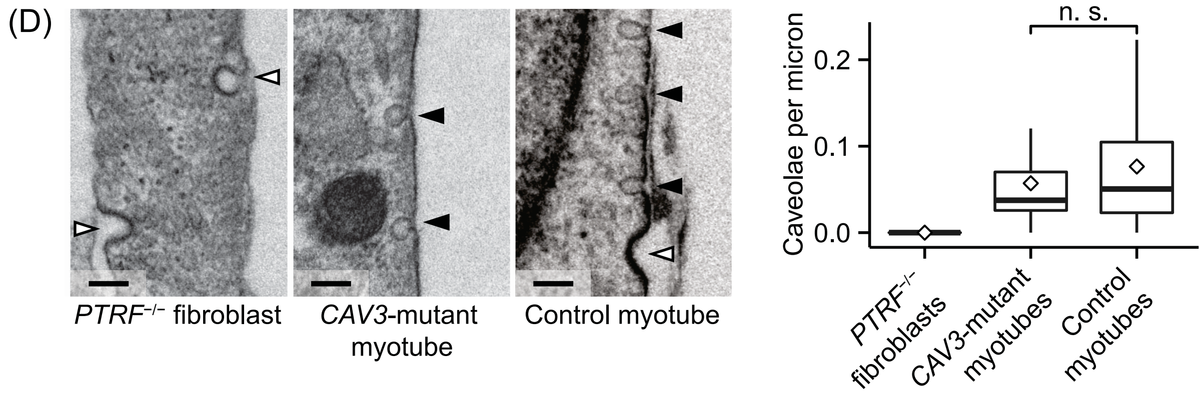
(D)
PTRF−/− fibroblast
CAV3-mutant myotube
Control myotube
n. s.
Caveolae per micron
0.2
0.1
0.0
PTRF−/− fibroblasts
CAV3-mutant myotubes
Control myotubes

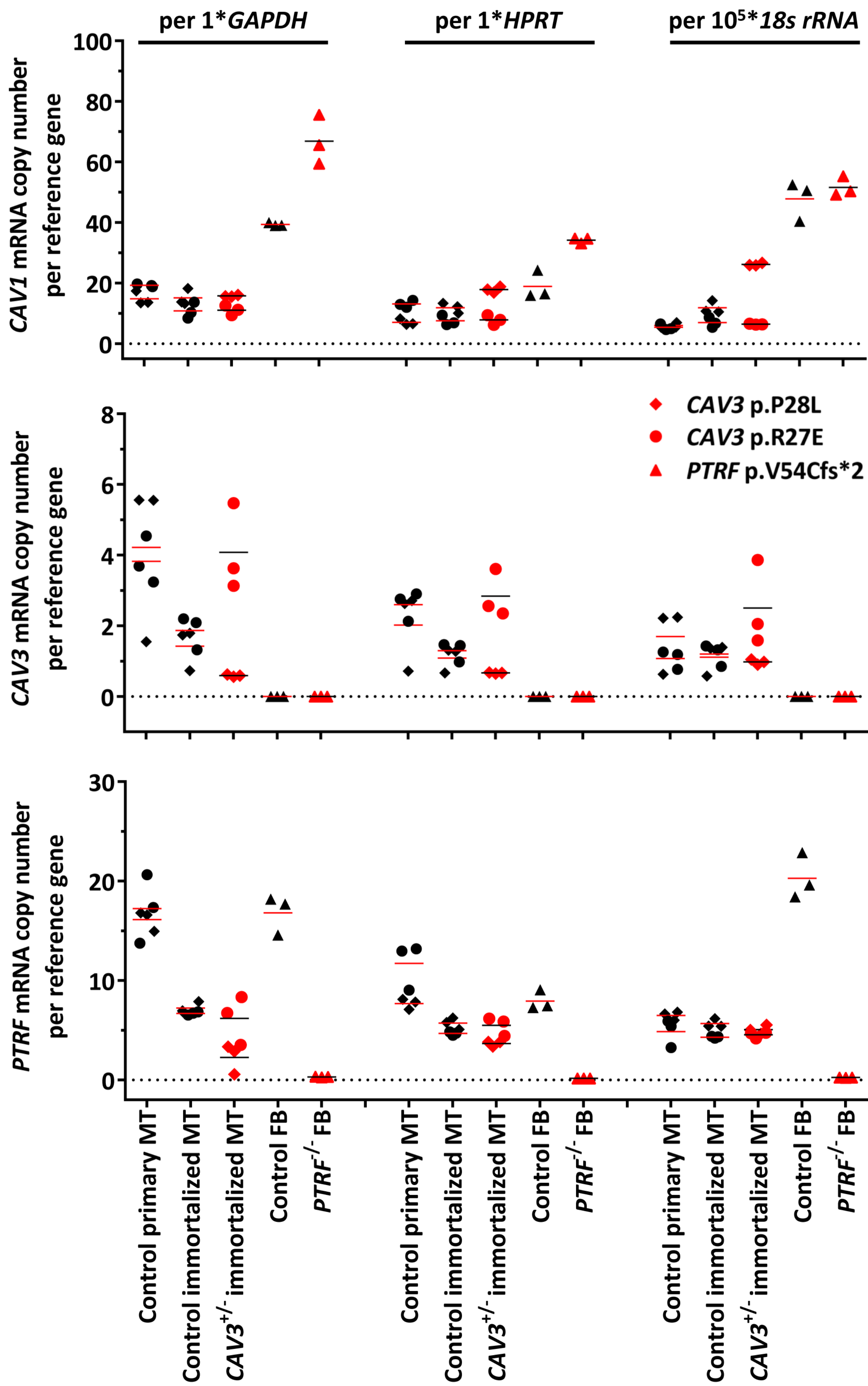

per 1*GAPDH
per 1*HPRT
per 10⁵*18s rRNA
CAV1 mRNA copy number per reference gene
CAV3 mRNA copy number per reference gene
PTRF mRNA copy number per reference gene
CAV3 p.P28L
CAV3 p.R27E
PTRF p.V54Cfs*2
Control primary MT
Control immortalized MT
CAV3+/- immortalized MT
Control FB
PTRF-/- FB

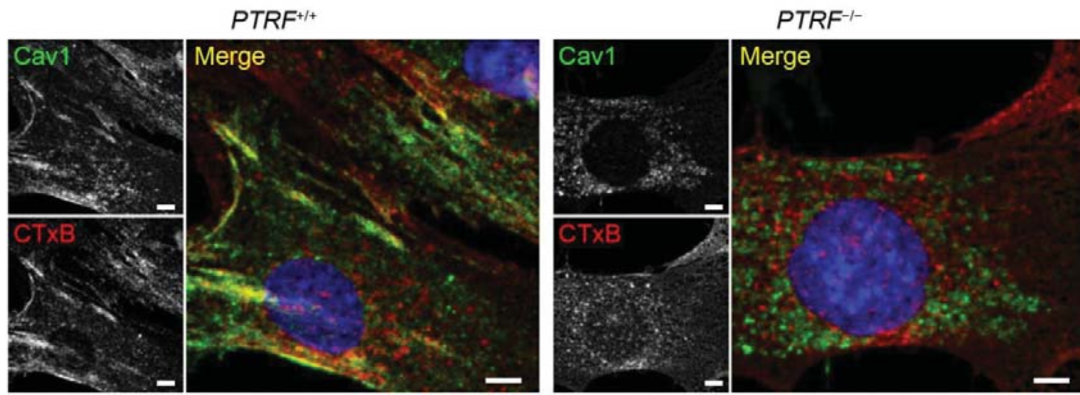
PTRF+/+
Cav1
Merge
CTxB
PTRF−/−
Cav1
Merge
CTxB

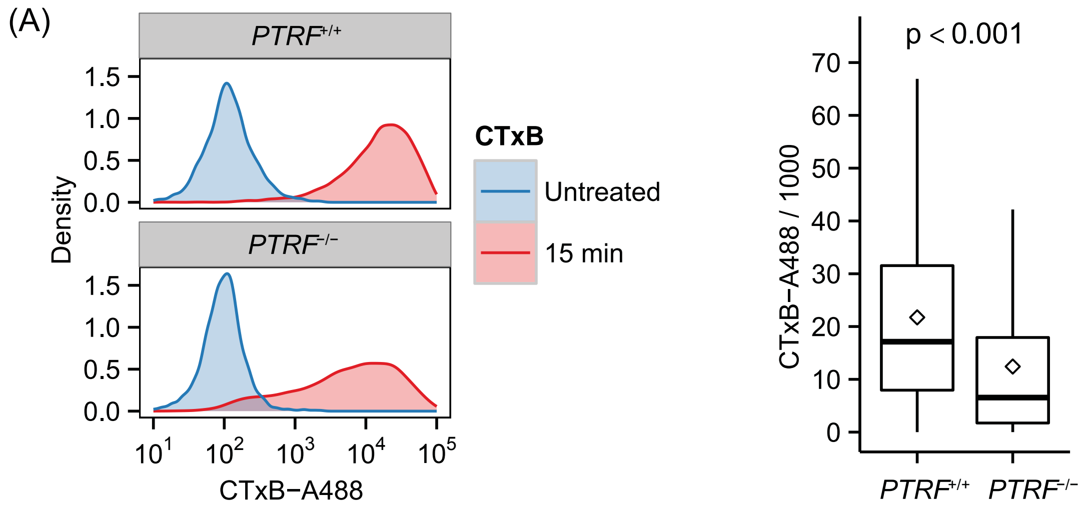
(A)
PTRF+/+
PTRF−/−
1.5
1.0
0.5
0.0
Density
CTxB
Untreated
15 min
CTxB−A488
p < 0.001
70
60
50
40
30
20
10
0
CTxB−A488 / 1000
PTRF+/+
PTRF−/−

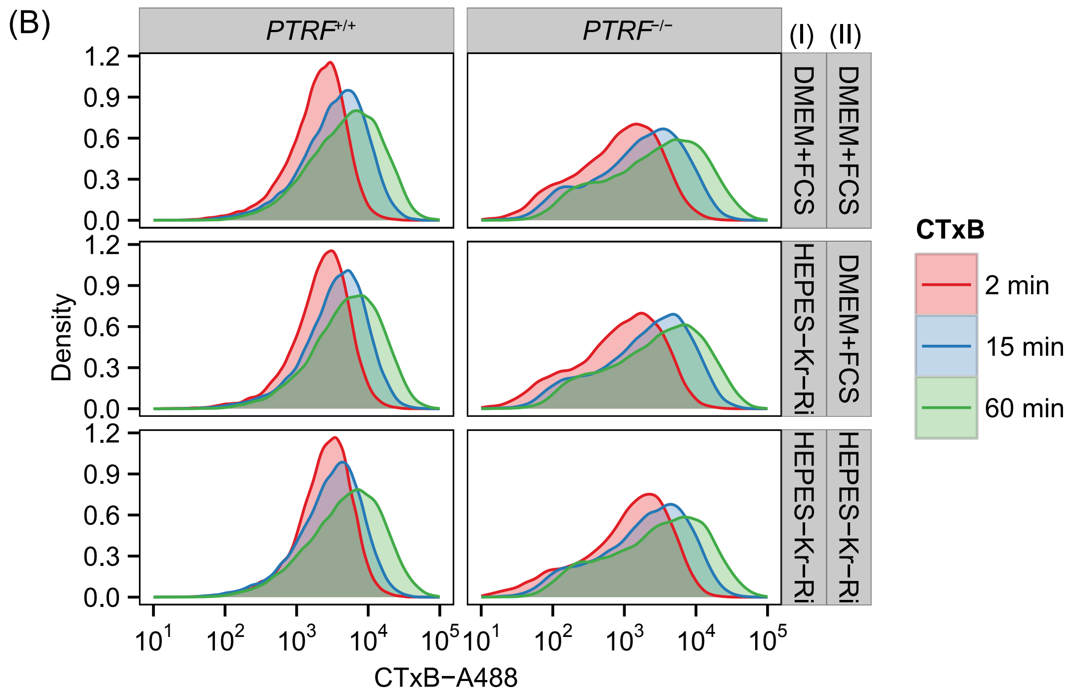
(B)
PTRF+/+
PTRF−/−
(I)
(II)
DMEM+FCS
HEPES−Kr−Ri
1.2
0.9
0.6
0.3
0.0
Density
CTxB
2 min
15 min
60 min
CTxB−A488

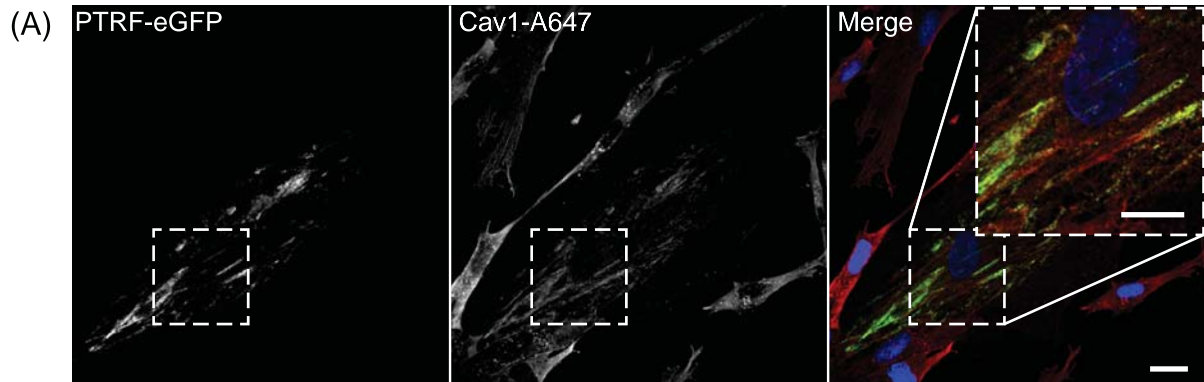
(A)
PTRF-eGFP
Cav1-A647
Merge

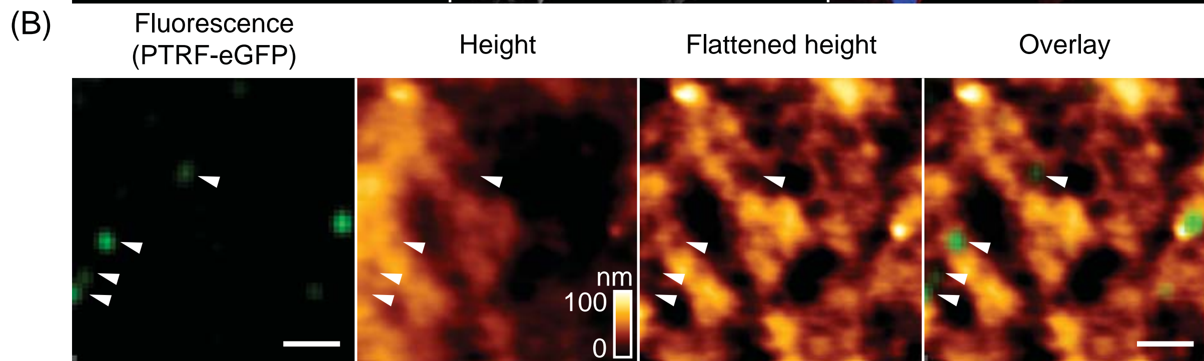
(B)
Fluorescence
(PTRF-eGFP)
Height
Flattened height
Overlay
nm
100
0

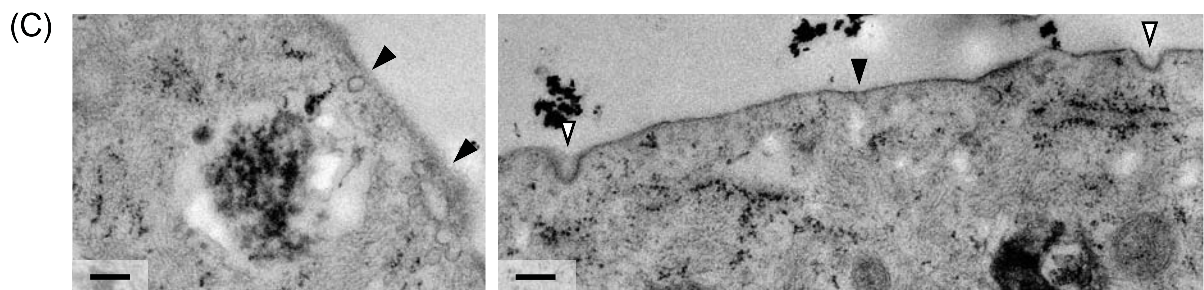
(C)

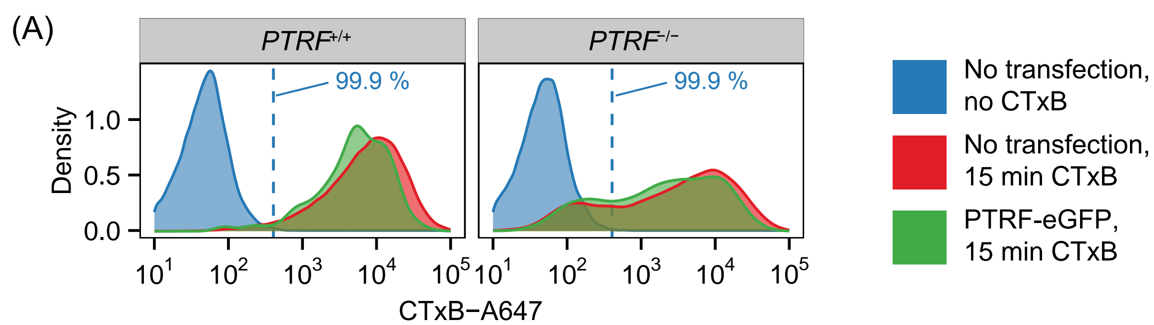
(A)
PTRF+/+
PTRF−/−
99.9 %
99.9 %
Density
1.0
0.5
0.0
10^1 10^2 10^3 10^4 10^5
CTxB−A647
No transfection, no CTxB
No transfection, 15 min CTxB
PTRF-eGFP, 15 min CTxB

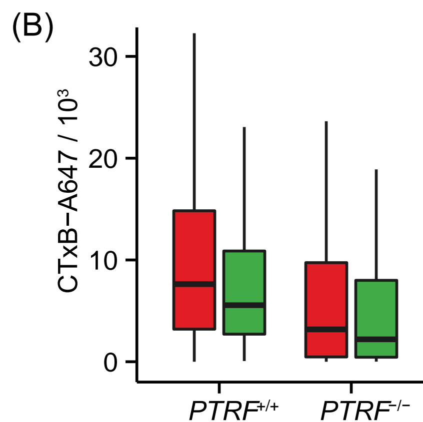
(B)
CTxB−A647 / 10^3
30
20
10
0
PTRF+/+
PTRF−/−

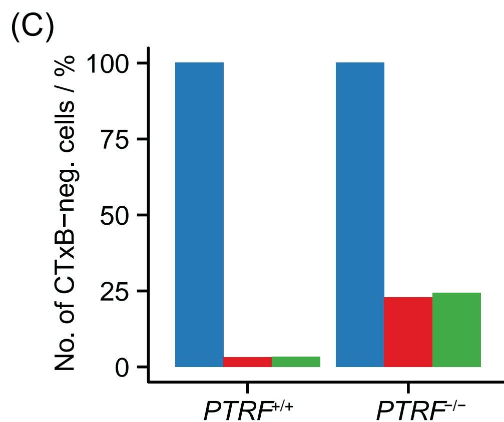
(C)
No. of CTxB−neg. cells / %
100
75
50
25
0
PTRF+/+
PTRF−/−